J Biol Phys (2013) 39:343–362
DOI 10.1007/s10867-012-9293-5

ORIGINAL PAPER

Conformational properties of interacting neurofilaments: Monte Carlo simulations of cylindrically grafted apposing neurofilament brushes

Lakshmi Jayanthi · William Stevenson · Yongkyu Kwak · Rakwoo Chang · Yeshitila Gebremichael

Received: 20 July 2012 / Accepted: 4 November 2012 / Published online: 13 December 2012

Abstract Neurofilaments are essential cytoskeletal filaments that impart mechanical stability to axons. They are mostly assembled from three neurofilament proteins that form the core of the filament and its sidearms. Adjacent neurofilaments interact with each other through their apposing sidearms and attain unique conformations depending on the ionic condition, phosphorylation state, and interfilament separations. To understand the conformational properties of apposing sidearms under various conditions and gain insight into interfilament interactions, we performed Monte Carlo simulations of neurofilament pairs. We employed a sequence-based coarse-grained model of apposing NF sidearms that are end-tethered to cylindrical geometries according to the stoichiometry of the three neurofilament subunits. Monte Carlo simulations were conducted under different conditions such as phosphorylation state, ionic condition, and interfilament separations. Under salt-free conditions, apposing sidearms are found to adopt mutually excluding stretched but bent away conformations that are reminiscent of a repulsive type of interaction. Under physiological conditions, apposing sidearms are found to be in a coiled conformation, suggesting a short-range steric repulsive type of interaction. Increased sidearm mutual interpenetration and a simultaneous decrease in the individual brush heights were observed as the interfilament separation was reduced from 60 to 40 nm. The observed conformations suggest entropic interaction as a likely mechanism for sidearm-mediated interfilament interactions under physiological conditions.

Electronic supplementary material The online version of this article (doi: 10.1007/s10867-012-9293-5) contains supplementary material, which is available to authorized users.

L. Jayanthi · W. Stevenson · Y. Gebremichael (✉)
Department of Biomedical Engineering, Wayne State University, Detroit, MI 48201, USA
e-mail: yeshig@wayne.edu

Y. Kwak · R. Chang
Department of Chemistry, Kwangwoon University, Seoul 139–701, Republic of Korea

Keywords Neurofilament sidearms · Phosphorylation · Monte Carlo simulation · Neurofilament brush model · Polyampholytes

1 Introduction

Neurofilaments (NFs) are the most abundant structural element in large myelinated axons (see Fuchs and Cleveland [1] and Lee and Cleveland [2] for review). They belong to the type IV intermediate filaments, and play a major role in maintaining the structural stability of the axon of vertebrate neurons [2–4]. NFs constitute the major part of the axonal cytoarchitecture and regulate the radial axonal growth that is essential for maintaining proper conduction velocity [5–7]. The aberrant cytoskeletal organization of NFs, on the other hand, is considered to be responsible for various neurodegenerative diseases. For example, the abnormal behavior (such as accumulation or abnormal phosphorylation) of NFs has been associated with neurodegenerative diseases such as amyotrophic lateral sclerosis [8, 9], Parkinson's [10], Charcot-Marie-Tooth type 2E [11], giant axonal neuropathy [12], and Alzheimer's diseases [13, 14].

Structurally, NFs are obligate heteropolymers that are mostly assembled from three distinct molecular mass proteins known as neurofilament light (NF-L; 66 kDa), medium (NF-M; 95–100 kDa), and heavy (NF-H; 110–115 kDa) [2, 15]. More recently, α-internexin and perpherin were identified as the fourth subunit of NF's belonging to CNS and PNS, respectively [16, 17]. Each of these subunits is characterized by a common non-α-helical N-terminal head domain and a carboxyl terminal tail domain flanking a central α-helical rod domain that consists in $\sim$310 amino acids [4, 7, 15]. In human NFs, the central rod domain of the NF-L subunit polymerizes with the other two subunits as well as another NF-L subunit [18] (i.e., only NF-L can homopolymerize, while the other subunits dimerize by associating with NF-L) to form coiled-coil dimers that further assemble into tetramers [19]. It is worth mentioning that there is a mixed viewpoint on the subject of NF-L homopolymerization in other species, especially mouse and rat [18–22]. The tetramers in turn assemble in a half-staggered fashion to form a protofibril that leads to the formation of a mature 10-nm-diameter filamentous rod (core) [19]. The carboxyl terminal tails of the NF proteins project from the surface of the filament core to constitute the long unstructured sidearm protrusions. The core of the filament along with the sidearm protrusions forms the core-shell structure that constitutes the axonal cytoskeletal network.

The C-terminal tails of the three subunits have varying chain lengths (ranging from 142 amino acids in NF-L subunits to $\sim$600 amino acids in NF-H subunits) that are abundant with charged amino acid residues. The polypeptide chains attain more negative charges upon phosphorylation of the lysine-serine-proline (KSP) repeat motifs that are particularly found in the NF-M and NF-H sidearms. Both NF-L and NF-M sidearms have excess negative charges, behaving more as negatively charged polyampholytes. On the other hand, NF-H sidearms are nearly neutral under dephosphorylated conditions, behaving as neutral polyampholytes. Upon phosphorylation, NF-H sidearms also become negatively charged polyampholytes due to the excess negative charges from the KSP phosphorylation. These behaviors inspired the treatment of NF sidearms as polyampholyte brushes in many recent studies [23–25].

Being polyampholytic in nature, the NF sidearms exhibit dynamic conformations in response to changes in physiological conditions such as ionic strength, pH, and phosphorylation states. An important issue on this subject is related to the nature of the

conformational changes of NF sidearms in the presence of neighboring filaments. NF sidearms are considered to be vital for mediating the interactions between neighboring filaments, and insight into the NF interactions can be gained through examining the conformational characteristics of apposing sidearms. The present study employs the model of a pair of NF brushes to reveal the conformational properties of apposing sidearms under various conditions. Such conformational analysis can be helpful in providing insight into the mechanism behind sidearm-mediated NF interactions, a subject that is not yet fully understood.

In the past, different studies have employed conformational analysis to shed light on to the nature of interacting polyelectrolyte brushes [26, 27]. For example, Cao et al. employed a coarse-grained bead spring polymer brush model to computationally study the conformational characteristics of polyelectrolyte brushes that are end-grafted to two apposing planar surfaces [26]. A similar study investigated a pair of spherical polyelectrolyte brushes (SPEs) to assess the behavior of chain conformations when subjected to compression under low- and high-ionic concentration solutions [27]. Both studies revealed coiled conformations under high-ionic concentrations, giving insight into the dynamic properties of polyelectrolyte brushes under ionic conditions.

Compared to pure polyelectrolyte brushes, the nature and charge distribution of NF sidearms provide a rich conformational behavior that may play an important role in controlling the interactions between neighboring filaments. Such behavior was addressed by the recent work of Stevens et al. who examined the interactions between apposing NF sidearms that are grafted to planar surfaces [23]. The study revealed that the sidearms adopt a condensed conformation and exhibit significant interdigitation upon compression of the walls. In our study, a model of cylindrically grafted apposing NF sidearms was treated to reveal the conformational properties of interacting NFs. The model comprises cylindrically grafted polypeptide chains representing the 10-nm-diameter NF cores and polyampholyte sidearm chains that are end-tethered to the cores according to the stoichiometry of the three NF subunits. Given the subunit stoichiometry and the morphology of native NFs, a model of polypeptide chains that are grafted to cylindrical backbones (according to the NF stoichiometry) is expected to yield useful insight into interacting NFs.

We present in the following the computational study of interacting NF pairs under various conditions. The paper is organized as follows: Section 2 describes the model and simulation methods of the study. Further details on the NF brush model can be found in Chang et al. [25]. Section 3 presents the results of the computational study, which is followed by the Discussion and Conclusion section (Section 3.1).

2 Methods

2.1 Model

In our previous computational studies of a single NF brush, we explored the conformational behavior of sidearms in an isolated NF by means of a sequence based coarse-grained (CG) model of the NF brush [25, 28]. The model comprises cylindrical geometry representing the 10-nm-diameter NF core and polyampholyte sidearm chains that are tethered to the cylindrical core according to the stoichiometry of the NF subunits. Here, we extend this model to a pair of cylindrically grafted apposing NFs in order to characterize the conformational changes of NF sidearms in the presence of interacting adjacent filaments.

The C-terminal tails or sidearms of the two filaments are modeled as flexible chains consisting in a collection of CG sites or hard spheres of diameter σ_s = 0.6 nm, where each CG site represents the polypeptide chain at amino acid resolution. A total of 31 sidearms were tethered to each filament core according to the stoichiometric ratio NF-L: NF-M: NF-H of 7:3:2. In each filament, the sidearms are equally spaced along the z-axis of the backbone but grafted randomly around the core. The stoichiometry, charge distribution, and sequences of the C-terminal tails are modeled to represent the human NF sequence as described in Chang et al. [25].

In the present model, the NF cores of the two filaments are placed in a box of dimensions 400 nm × 400 nm × 50 nm equidistant from the center of the box, with the filaments axes aligned along the z-axis. The interfilament distance is set by adjusting the distance between the centers of the 10-nm-diameter cylindrical cores. Different interfilament separations ranging from 40 to 60 nm were selected and Monte Carlo (MC) simulations of NF pairs were performed for each interfilament separation. In these simulations, the apposing NFs were first equilibrated at 60 nm separation and then gradually compressed towards 40 nm by reducing the distance between the centers of apposing filaments by 1.25 nm per step. At each stage, the pair is fully equilibrated before further reduction in distance or another production run takes place. The equilibrated configuration is then used to generate the next configuration with a smaller separation. This is repeated until the interfilament distance of 40 nm is reached.

The MC simulations were carried out under both phosphorylated and dephosphorylated conditions at salt-free and 150 mM ionic concentrations. To simulate the effect of phosphorylation, negative charges of $-2e$ were assigned to the serine residues of the KSP repeat motifs in the NF-M and NF-H sidearms, whereas the serine residues were kept neutral for the dephosphorylated conditions. Similar to the isolated NF brush model [25], monovalent K^+ ions were added to the system to maintain the charge neutrality of the whole system in the salt-free conditions. The interaction potential between different objects is treated as the sum of the hard sphere (or rod) and electrostatic interactions. The hard sphere (or rod) interaction $U_{hs}\left(r_{ij}\right)$ is given by

$$U_{hs}\left(r_{ij}\right) = \begin{cases} \infty & r_{ij} \leq \sigma_{ij} \\ 0 & otherwise \end{cases} \tag{1}$$

where r_{ij} is the distance between the centers of two objects i and j and $\sigma_{ij} = \frac{\sigma_i + \sigma_j}{2}$.

Under salt-free conditions, the electrostatic interaction potential $U_{el}\left(r_{ij}\right)$is given by

$$U_{el}\left(r_{ij}\right) = \frac{e^2 Z_i Z_j}{4\pi\,\varepsilon_0 \varepsilon\, r_{ij}} \tag{2}$$

where e, ε_0, and ε are the electric charge, vacuum permittivity, and the dielectric constant of a solution, respectively, and Z_i is the charge valence of a coarse-grained site i. The electrostatic potential $U_{el}\left(r_{ij}\right)$ can be expressed in terms of the Bjerrum length l_B as:

$$\frac{U_{el}\left(r_{ij}\right)}{k_B T} = \frac{l_B Z_i Z_j}{r_{ij}} \tag{3}$$

where $l_B = \frac{e^2}{4\pi\varepsilon_0 \varepsilon k_B T}$ (k_B is the Boltzmann constant and T is the system temperature). The Bjerrum length l_B is the separation at which the electrostatic interaction between two elementary charges is comparable in magnitude to the thermal energy scale $k_B T$ and is around 0.7 nm for water at T = 300 K.

In the physiological condition, the ionic concentration is incorporated into the model implicitly by the use of the screened Coulomb (Debye-Hückel) potential given by

$$\frac{U_{el}\left(r_{ij}\right)}{k_B T} = l_B Z_i Z_j \frac{e^{-\kappa r_{ij}}}{r_{ij}} \tag{4}$$

where κ is the inverse Debye screening length [29] given by

$$\kappa^{-1} = \sqrt{\frac{\varepsilon_0 \varepsilon k_B T}{2 N_A e^2 I}}. \tag{5}$$

Here, N_A is the Avogadro number and I is the ionic strength (M). All other variables are the same as defined above. In terms of the Bjerrum length l_B, κ can be written as:

$$\kappa^{-1} = \sqrt{\frac{1}{8\pi l_B N_A I}}. \tag{6}$$

2.2 Simulation procedure

The present study adopts the simulation procedure described in Stevenson et al. [28]. The study employs the standard canonical ensemble (NVT i.e., constant number N of particles, volume V and temperature T) of MC simulations. The standard MC moves, including crankshaft, continuum configuration bias, and random rotation are applied to the sidearm chains. As discussed in Stevenson et al. [28], the trial moves are implemented in a two-step process. Initially, the move is checked to avoid an overlap with other particles. If this condition is satisfied, the change in electrostatic energy, ΔU,associated with the move is calculated by using the Ewald summation method [30]. The trial move is accepted or rejected according to the probability of $\exp\left(-\Delta \mathrm{U} / (\mathrm{k_B T})\right)$, where k_B is the Boltzmann constant and T is the absolute temperature (K).

As described in Stevenson et al., the simulation was performed in a three-step process (see Stevenson et al. [28] for more details). However, for sufficient equilibration under each condition (phosphorylation state, proximity, ionic strength), the system was equilibrated for three times the equilibration steps needed for a single filament. In other words, 3×10^6 MC steps were performed under each condition before the last equilibrated simulations of 10^6 steps were carried out as a production run for sampling the average properties. All average properties were calculated from the equilibrated configurations that were sampled at every 1,000 MC steps of the production runs. For sufficient statistics, the monomer density profile, average interpenetration (I), and average brush height (h) were determined from six independent simulations that were initialized differently. The data presented here represent the average of data collected from six simulations except for the last two distances (i.e., 45 and 42.5 nm), where it was averaged over four simulations. The use of four independent simulations (instead of six) for averaging at these two distances was due to the challenge in fully equilibrating the NF pairs as the interfilament separation decreases.

3 Results

In the present study, we set out to reveal the conformational behavior of apposing sidearms of interacting adjacent NFs. To this end, we performed off-lattice MC simulations of NF pairs, which comprise apposing sidearms end-tethered to cylindrical geometry cores. The

study was done at different interfilament separations ranging from 60 to 40 nm. In the first step, a number of independent NF pair simulations were carried out at 60 and 40 nm separations. Then the interfilament distance of each independent simulation was reduced in small steps from 60 nm towards 40 nm.

The choice for the range of interfilament distance was partly motivated by the range of reported NF spacing. In the literature, various interfilament separations (40–60 nm [31], 35–40 nm [32], and 33–48 nm [33]) have been reported under normal physiological conditions. Note that, in our model, the interfilament distances are measured from the centers of the 10-nm-diameter backbones. Therefore, the selected range corresponds to 30–50 nm from the filament surfaces, which is nearly within the reported physiological ranges.

At the two extreme interfilament separations (60 and 40 nm), MC simulations of NF pair were conducted under different conditions, i.e., phosphorylation states and ionic conditions. First, in order to gain insight into the role of electrostatic repulsions on the conformation and interactions of apposing sidearms, the MC simulations were performed under salt-free conditions. The results from these simulations were then compared with similar simulations under physiological ionic conditions.

The simulations under the physiological ionic conditions were continued for interfilament distances from 60 to 40 nm under both phosphorylation states. The conformational changes arising from different factors were then examined using measures such as the average brush height, mutual interpenetration, and density profile. Examination of the conformational characteristics of apposing sidearms resulting from these analyses will allow us to gain insight into the nature of sidearm interactions under different conditions.

3.1 Conformations of apposing NF sidearms under salt-free conditions

It is known that the phosphorylation of NF sidearms at their KSP repeat motifs modifies the charge distribution of both NF-M and NF-H sidearms and increases their lateral extension [34, 35]. In view of this, it was hypothesized that phosphorylation plays a key role in specifying the interfilament separation [36, 37]. Central to this hypothesis is that the interfilament interaction is governed by sidearm-mediated electrostatic repulsion that arises from the net negative charge [38]. Clearly, such repulsive interaction is expected to manifest itself in the conformational characteristics of apposing sidearms. To observe the conformations arising from sidearm-mediated repulsive interactions, we performed MC simulations of an apposing NF brush under salt-free conditions, for both the phosphorylated and dephosphorylated states. From the resulting conformation, one would be able to gauge the possibility of the repulsive type of interactions between apposing sidearms. Note that the salt-free conditions allow us to observe the effect of electrostatic interaction exclusively.

To observe the conformations arising from electrostatic interaction, we first visually inspect the structures of adjacent NFs by extracting representative snapshots of configurations from equilibrated MC simulations. Figure 1a and b depict typical snapshots of the NF brush pair at 60 nm separation. The figures present equilibrated conformations of the dephosphorylated (Fig. 1a) and phosphorylated (Fig. 1b) NF pairs under salt-free conditions. An interesting feature of these figures is that the sidearms from adjacent filaments are found to bend away from each other leaving a depletion region in between, a behavior suggestive of the repulsive type of interactions between apposing sidearms.

The difference between the dephosphorylated (Fig. 1a) and phosphorylated (Fig. 1b) NF pairs is seen only in the fine tuning present in the individual sidearms. In terms of the individual sidearms, while NF-L and NF-M adopt an extended conformation in both

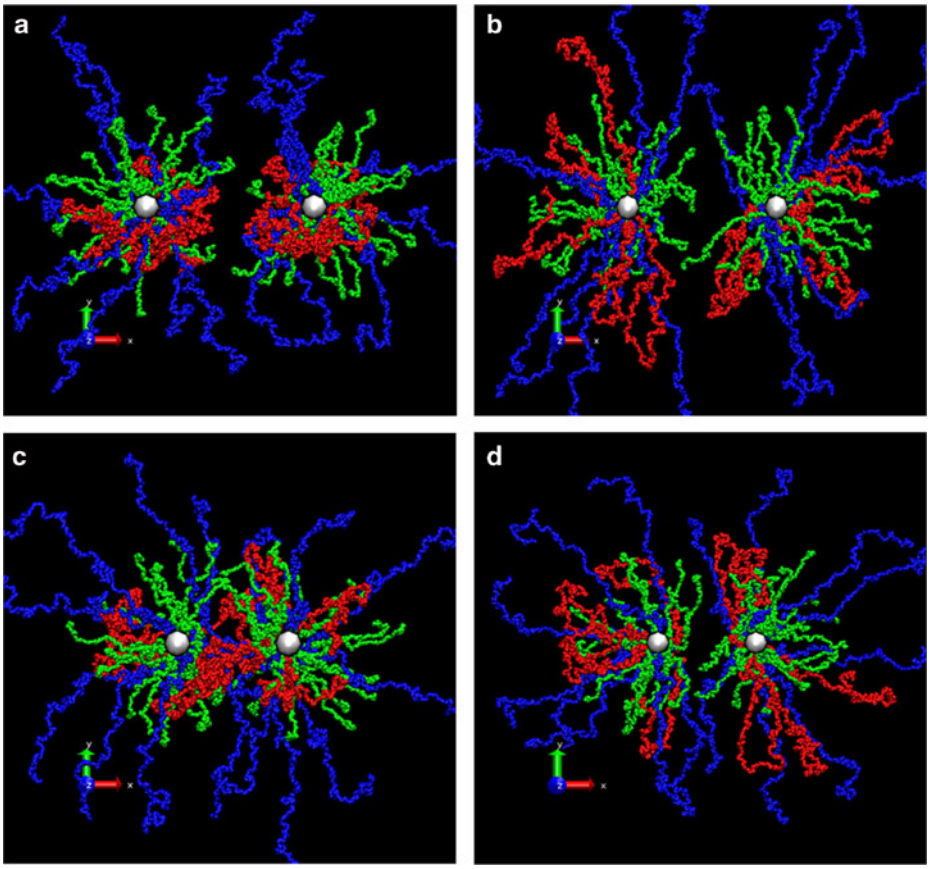

Fig. 1 Representative snapshots (*top view*) of a 60-nm-apart dephosphorylated (**a**) and phosphorylated (**b**) NF brush pair under salt-free conditions. Snapshots of a 40-nm-apart dephosphorylated (**c**) and phosphorylated (**d**) NF pair under salt-free conditions (color coding: NF-L – *green*; NF-M – *blue*; NF-H – *red*)

phosphorylation states, NF-H sidearms exhibit significant changes in their conformation upon change of the phosphorylation condition. Under dephosphorylated conditions, NF-H sidearms are collapsed around their own filament core, with little to no influence on sidearms from the adjacent filament. In contrast, phosphorylated NF-H sidearms adopt an extended conformation with a ring-like structure at their free ends and participate in the repulsive interactions (see also Supplementary Fig. 1, in which NF-L was deleted to clearly depict the repulsive behavior of the longer sidearms).

To observe the effect of proximity on the interacting sidearms, similar MC simulations were performed at 40 nm interfilament separations. Figure 1c and d represent the behavior of apposing NFs under salt-free conditions when the centers of the filament cores are 40 nm apart. At this separation, one observes a slight difference between the dephosphorylated (Fig. 1c) and phosphorylated (Fig. 1d) states. In the phosphorylated state, except for the reduction in the depletion region, the apposing sidearms still exhibit a conformation that is indicative of a repulsive type of interaction (cf. Fig. 1d). In contrast, dephosphorylated

NF pairs exhibit a mixed behavior in which the collapsed NF-H sidearms have become mutually interpenetrated, while the other two types of sidearms are expelled out, exhibiting a partially repulsive behavior.

Taken together, under salt-free conditions, NF sidearms from adjacent filaments exhibit conformational characteristics that are reminiscent of a repulsive type of interaction as suggested in the literature [38, 39]. However, as presented below, this conformational behavior changes significantly when the simulations are performed under ionic solutions, possibly due to a different interaction mechanism.

3.2 Conformations of apposing NF sidearms under physiological conditions

The simulations under salt-free conditions reveal the conformational behavior of apposing sidearms that can be attributed to the repulsive electrostatic type of interactions. To observe the conformational properties under physiological conditions, we performed MC simulations of adjacent NFs under 150 mM ionic solutions. As commonly practiced in the simulations of polyelectrolyte systems (Panwar and Kumar et al. [40] and references therein), the ionic strength is incorporated into the model implicitly through the use of the Debye-Hückel screened Coulomb potential (cf. Methods section). For comparison with the salt-free conditions, the MC simulations were first performed at 60 nm and 40 nm interfilament separations under both phosphorylation conditions.

Figure 2a and b show typical snapshots of the 60-nm-apart adjacent NFs under 150 mM ionic conditions. The plots depict the equilibrium conformations of dephosphorylated (Fig. 2a) and phosphorylated (Fig. 2b) NF pairs. In sharp contrast to the salt-free conditions, the snapshots of the NF pair under physiological conditions reveal a coiled conformation for both phosphorylation conditions. Moreover, the difference between the phosphorylated and dephosphorylated NF pairs is not significant at 60 nm separations.

A qualitatively similar behavior was observed for the 40-nm-apart neighboring NFs (Fig. 2c, d). At 150 mM ionic concentration, the apposing sidearms adopt a coiled conformation for both phosphorylation states. However, similar to the salt-free conditions, relatively higher mutual interpenetration was observed at 40 nm separations when compared to the 60-nm separations.

The difference in the conformational properties of NF sidearms under 150 mM and salt-free conditions arises from the ionic screening present in the 150 mM ionic solution. In the presence of salt ions, the repulsive interaction observed under salt-free conditions will be screened, leading to a type of interaction that is dominated by short-range steric exclusion. When the proximity between the NF cores is reduced from 60 to 40 nm, the monomers in each sidearm rearrange themselves so as to relieve the short-range steric repulsions and eventually adopt a conformation with relatively higher interpenetrations.

3.3 Density profile of apposing neurofilaments

The above qualitative observations from visual inspection can be quantified through measures that reveal the average properties of sidearm conformation. One such measure is the cross-sectional number density profile $\rho(x,y)$ of monomers in apposing sidearms. $\rho(x,y)$ represents the mean distribution of monomers across a planar cross section normal to the longitudinal axes of the apposing filaments. At any position $\vec{X} \equiv (x, y)$ on the cross section,

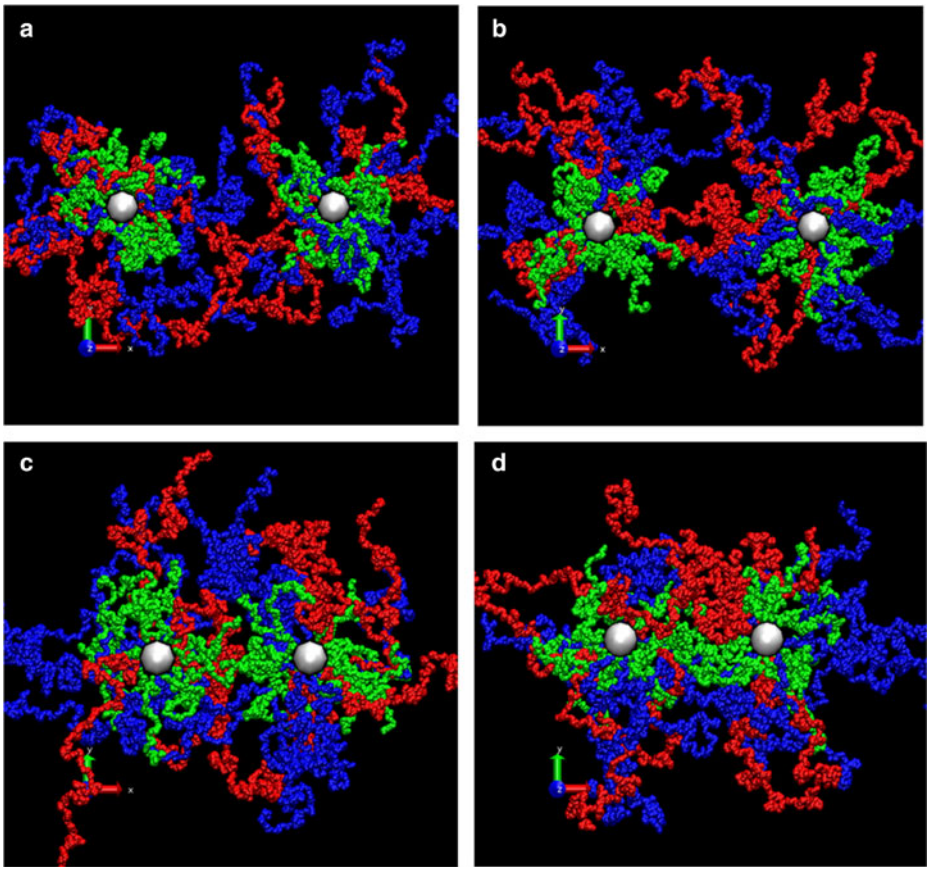

Fig. 2 Representative snapshots (*top view*) of a 60-nm-apart dephosphorylated (**a**) and phosphorylated (**b**) NF brush pair under physiological condition. Snapshots of a 40-nm-apart dephosphorylated (**c**) and phosphorylated (**d**) NF pair under physiological conditions

$\rho(x,y)$ is calculated by counting the number of monomers within the cross-sectional area between (x,y) and $(x + dx, y + dy)$ (for all depths along the longitudinal Z-axis) and then normalizing by the volume $dxdyL_z$. Here, L_z is the length of the simulation box along the filament longitudinal axis. Mathematically, $\rho(x,y)$ can be expressed as

$$\rho\,(x,\,y) = \frac{1}{dxdyL_z}\sum_{j}^{N_s}\left\langle \delta\left(\vec{X} - \vec{X}_j\right)\right\rangle. \tag{7}$$

The bracket $\langle ... \rangle$ represents the ensemble average and $\rho(x,y)$ is the ensemble average of 1,000 configurations sampled from 10^6 equilibrated MC simulations. The two-dimensional contour plots of the density profile obtained from this calculation, along with the visual data (snapshots), allow us to predict the spatial arrangement of apposing sidearms.

Figure 3a and b show the contour plots of $\rho(x,y)$ for the NF pair under salt-free conditions. The plot presents the average cross-sectional density profiles of 60-nm-apart dephosphorylated (Fig. 3a) and phosphorylated (Fig. 3b) NF pairs. The plots clearly

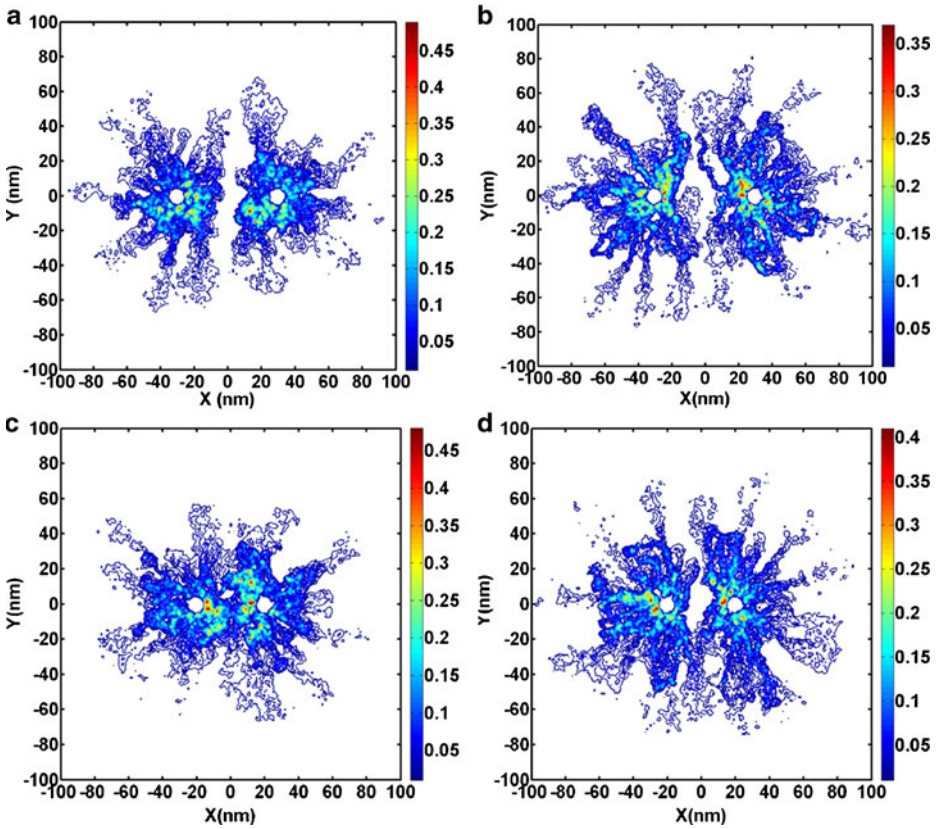

Fig. 3 Two-dimensional contour plots of the average cross-sectional density profile $\rho(x, y)$ of the 60-nm-apart dephosphorylated (**a**) and phosphorylated (**b**) NF pair under salt-free conditions. Similar contour plots of $\rho(x, y)$ for the 40-nm-apart dephosphorylated (**c**) and phosphorylated (**d**) NF pair under salt-free conditions

demonstrate that the monomers from one filament are forced to bend away from those of the apposing filament. The monomers in the apposing sidearms are expelled from the central region, forming a depletion region around the center. A similar behavior was observed for the 40-nm-apart NF pairs under salt-free conditions. Figure 3c and d represent the average cross-sectional density profiles of 40-nm-apart dephosphorylated and phosphorylated NF pairs, respectively, under salt-free conditions. While the 40-nm-apart dephosphorylated NF pairs show marginal overlapping near the center, the average density profile of the 40-nm-apart phosphorylated apposing sidearms exhibit little mutual interpenetration.

To assess the conformational properties of interacting neurofilaments under physiological conditions and then compare with the salt-free conditions, we calculated the average density profile $\rho(x,y)$ of 40 nm and 60 nm apart NF pairs under 150 mM ionic solutions. Figure 4a and b depict the contour plots of $\rho(x,y)$ for 60 nm and 40 nm apart, respectively, phosphorylated NF pairs under physiological conditions. In contrast to the salt-free conditions, the plots reveal the coiled conformations of the apposing sidearms.

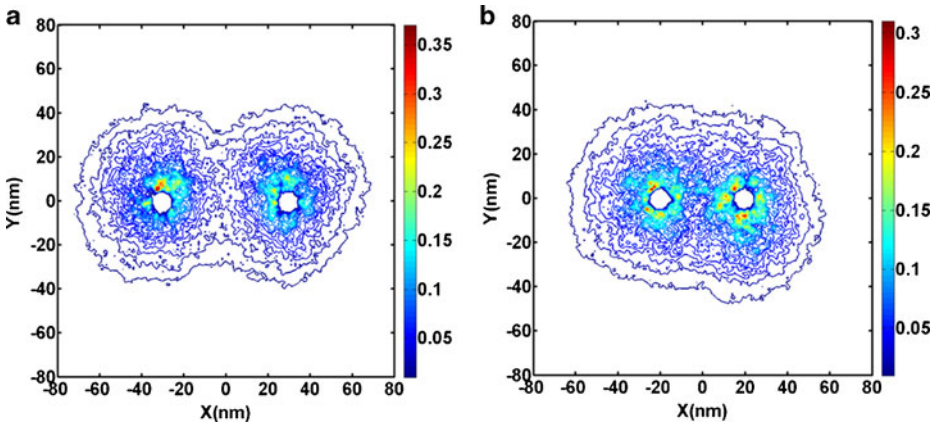

Fig. 4 The two-dimensional contour plots of the average cross-sectional density profile $\rho(x, y)$ of the 60-nm-apart (**a**) and 40-nm-apart (**b**) phosphorylated NF pair under physiological condition

Additionally, a noticeable conformational difference was observed between the 40-nm and 60-nm-apart NF pairs.

At the 60 nm separations, the density profile reveals that the apposing sidearms aggregated around their own filament core, with marginal overlapping at the center. On the other hand, relatively higher overlapping or interpenetration is observed in the density profile of 40-nm-apart NF pairs. With regard to the phosphorylation state, no significant difference was observed in the density profiles of dephosphorylated and phosphorylated NF pairs for both interfilament separations (data not shown).

An interesting observation from the contour plots depicted in Fig. 4 is that the monomer densities are significantly concentrated around the core of each filament (refer to the scale). Even at 40 nm separations, where a relatively higher overlap is observed under physiological conditions, the central region between the cores shows only a fraction of the overall density profile. Clearly, the cylindrical geometry allows the sidearms to surround the curvature of the backbone in an effort to retract from the apposing sidearms. A similar behavior was reported by a study that investigated the polymer-mediated interactions between nanorods [41]. In this report, the polymeric chains that are end-tethered to the cylindrical rods escape from the central narrow region to surround the curvature, decreasing the force between approaching structures. This observation points to the importance of proper geometry in accessing available configurational space that relieves steric repulsion between monomers from adjacent filaments.

In general, the average density profile of apposing sidearms under salt-free conditions reveals no significant overlapping or interpenetration, suggesting a repulsive type of interaction under this condition. In contrast, under physiological conditions, the electrostatic interaction observed in the salt-free conditions is screened by the presence of salt ions, leading to a short-range steric exclusion type of interaction. Furthermore, when the proximity between the NF cores is changed from 60 nm to 40 nm, the monomers in each sidearm rearrange themselves so as to relieve the local steric repulsions, adopting a conformation with a relatively higher overlapping density profile.

3.4 Mutual interpenetration of apposing sidearms

The conformational properties discussed above reveal the mutually exclusive behavior of apposing sidearms in the salt-free condition, while some level of overlapping or mutual interpenetration was observed at 150 mM ionic solution. To assess the level of interpenetration under physiological condition, we define a conformational measure that quantifies the degree of mutual interpenetration or overlapping probability as described below. Furthermore, to reveal the changes in the level of mutual interpenetration as the interfilament separation decreases, we performed MC simulations of NF pairs by gradually reducing the interfilament distance from 60 nm towards 40 nm. In this process, starting from the equilibrated configuration at 60 nm separations, each filament is displaced by 1.25 nm towards the opposing filament, resulting in a total reduction of 2.5 nm in interfilament separation. The NF pair is then fully equilibrated at the new separation before subsequent production runs are performed for data collection. At the same time, the last configuration from the equilibration stage is taken as the starting configuration for the following compression step. This process was repeated systematically to gradually reduce the interfilament distance to 40 nm. The change in the overlapping probability arising from gradual compression of adjacent filaments was analyzed from the equilibrated data as detailed below.

3.4.1 Overlapping probability

To estimate the interpenetration between adjacent filaments, we define an averaged quantity I that measures the overlapping or interpenetration probability of apposing sidearms. For any given condition (interfilament separation, ionic strength, or phosphorylation states), we define I as the probability of finding monomers from one filament in the opposite half-side of the region between the two filaments. The opposite half-side corresponds to the (intermediate) region between the backbones of the two filaments that is above the mid-point for the filament on the left and below the mid-point for the filament on the right.

Mathematically, this can be expressed as

$$I = \frac{\int_0^{R/2} \rho_2(x)\,dx + \int_{R/2}^{R} \rho_1(x)\,dx}{\int_0^{R} \rho(x)\,dx}. \tag{8}$$

Where R is the interfilament separation. $\rho_j(x)$ is the number density of monomers from filament j that are found in the region between x and $x + dx$ at the intermediate region of the apposing filaments. Note that the x-axis is defined along the line joining the centers of the longitudinal axes of the filament cores. Conventionally, the longitudinal axes are selected along the z-axis and hence the y-z plane bisects the line joining the centers of the longitudinal axes. $\rho_j(x)$ is thus calculated from the number of monomers with in a small volume bounded by the y-z planes bisecting the x-axis at x and $x + dx$. The values obtained from numerically integrating $\rho_j(x)$ adjacent to the opposite filament are then normalized by the total number of monomers that are found in the region between the two filaments, i.e., those bounded by the y-z planes at $x = 0$ and $x = R$.

Figure 5 depicts the monomer density $\rho_j(x)$ of phosphorylated NF pairs for interfilament separations $R = 40$, 45, 50, 55, and 60 nm under physiological conditions. The plot shows that the average density $\rho_j(x)$ of the sidearms is concentrated near the backbone and

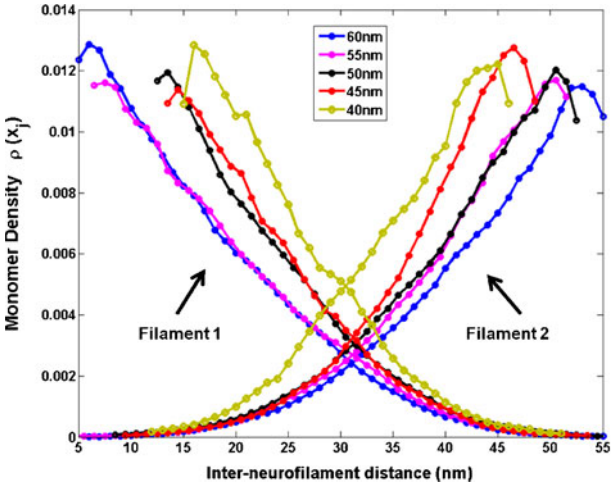

Fig. 5 The average density $\rho_j(x)$ of sidearm chain monomers as a function of the distance x from the surface of each filament j in a direction along the line normal to the filament axes. The plot shows the data for a 60, 55, 50, 45, and 40-nm-apart NF pair under physiological conditions

gradually decreases towards the opposite filament. The interpenetration of the sidearms in the central region is indicated by the overlapping monomer density profiles. As observed in the figure, the extent of the overlap increases as the backbones are compressed towards each other. The overlap/interpenetration is quantified by the interpenetration probability I, which was calculated by numerically integrating $\rho_j(x)$ of each filament beyond the mid-point. The value of I calculated from such analyses is then examined under different conditions.

Figure 6a–d present the overlapping or interpenetration probability I of adjacent NFs and the individual sidearms NF-L, NF-M, and NF-H, respectively, under physiological conditions for different phosphorylation states and interfilament proximity. First, as expected, a monotonically increasing overlapping probability was observed as the interfilament distance is decreased (Fig. 6a). For example, the interpenetration probability for the 60-nm-apart phosphorylated NFs is about $I = 0.07$, whereas a nearly 50% increase in I was observed as the interfilament separation is reduced from 60 to 40 nm (i.e., $I = 0.14$ at 40-nm separations). Using a planar grafted NF brush model, a similar monotonically increasing sidearm interpenetration behavior was observed by Stevens and Hoh as the opposing planar brushes are compressed towards each other [23].

Among the three NF sidearms, NF-L sidearms show the minimum overlapping probability, explained by their relatively shorter lengths (Fig. 6b) ($I \sim 0$ at 60 nm and increases exponentially to $I \sim 0.03$ as the interfilament distance decreases to 40-nm separations). In contrast, both NF-M (Fig. 6c) and NF-H (Fig. 6d) display a relatively higher overlap probability at 60 nm, a value that increases in a weak exponential manner with decreasing interfilament separations. As shown in the figure, all data have been fitted to exponential functions, where the goodness of the fit estimated based on the R^2 values are shown in the figure. In general, although a relative increase in overlapping probability was observed with a decrease in interfilament separations, compared to the number of monomers localized around or near the core of the backbone, the absolute number of overlapping or interpenetrating monomers is not large. Also, the difference in the overlapping behavior between phosphorylated and dephosphorylated states is not significant at the physiological conditions.

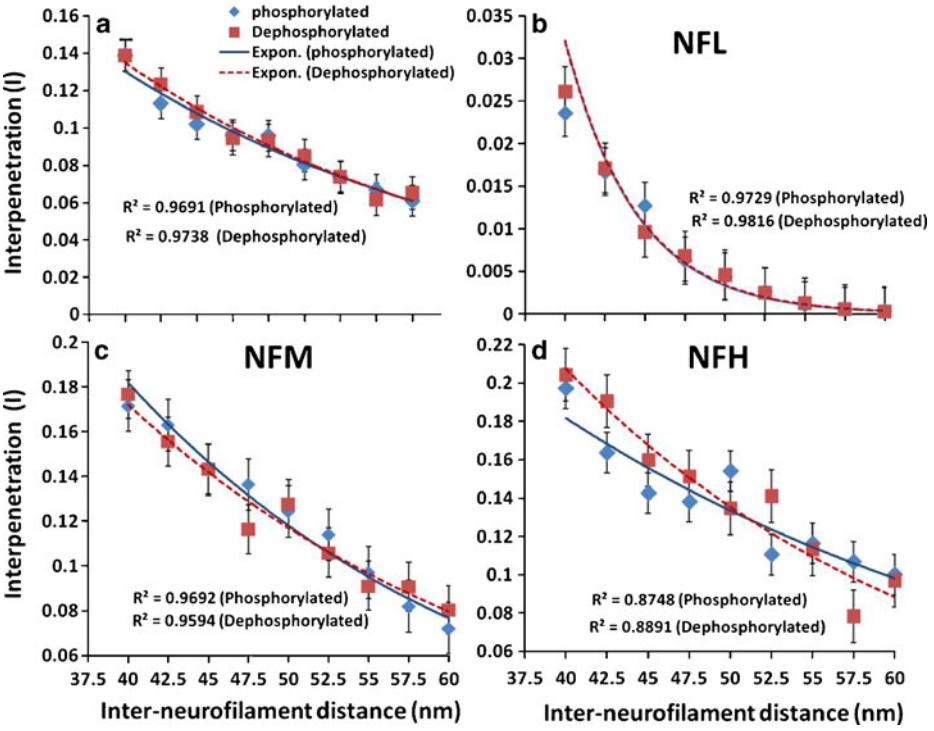

Fig. 6 The overlapping or interpenetration probability (I) of an adjacent NF brush as a function of interfilament separation under physiological conditions. The plot (**a**) shows the overall mutual interpenetration probability of the adjacent NF brush. (**b**–**d**) represents I for individual sidearms NF-L (**b**), NF-M (**c**) and NF-H (**d**) for dephosphorylated (■) and phosphorylated (♦) states. The data were fitted by exponential functions and are shown by a *dashed line* (–) for dephosphorylated and a *solid line* (-) for phosphorylated systems. The goodness of the fit for individual data as estimated by the R^2 value is shown in the figure. The error bar represents the standard error (SE) of the mean I value

3.5 Average NF brush height

Another useful quantity that captures the conformational behavior of NF sidearms is the height of the NF brush pair. The mean brush height $\langle x_j \rangle$ of a single filament j is determined by taking the first moment of monomer distribution as

$$\langle x_j \rangle = \frac{\int x_j \rho\left(x_j\right)}{\int \rho\left(x_j\right)} \tag{9}$$

where $\rho(x_j)$ is the number density of monomers in a small volume $dV\left(\equiv dxL_yL_z\right)$ at a distance x_j from the core of the filament j, in a direction towards the adjacent filament. Note again that the z-direction is along the longitudinal axis of the NF core and the brush height is measured in the x-direction. As we are interested in the brush height of the opposing filaments as they are facing each other, $\langle x_j \rangle$ is calculated based on the number density of the NF brush in the region between the two filaments. The average brush height of the two filaments is then calculated as: $h = \frac{\langle x_1 \rangle + \langle x_2 \rangle}{2}$.

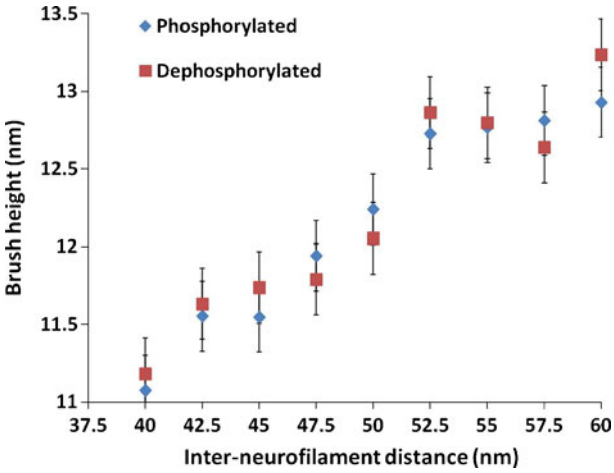

Fig. 7 The average brush height h of the dephosphorylated (■) and phosphorylated (♦) NF brush as a function of interfilament separation under physiological condition. The error bar represents the standard error (SE) of the mean h value

Figure 7 depicts the average brush height of the two filaments as a function of the interfilament distance under both phosphorylation states. The figure shows that monotonically decreases from 13.5 nm for the 60 nm separations to 11 nm for 40 nm separations, undergoing approximately a 20% reduction in size when the filaments are compressed from 60 nm to 40 nm. In terms of individual sidearms, NF-L does not show any particular pattern in its brush height, whereas both NF-M and NF-H sidearms mimic the pattern observed for the overall brush height (data not shown). Similar to the overlapping probability, under physiological conditions, the difference between dephosphorylated and phosphorylated systems is not significant. These results demonstrate the tendency of the NF brush to adopt a collapsed conformation (as demonstrated by the decrease in brush height) as the adjacent filaments approach each other. Although the mutual interpenetration between the brushes increases as they approach each other, the present result clearly shows that NF brushes shrink in height to retract themselves as the interfilament separation decreases.

4 Discussion and conclusion

In the present study, we investigated the conformational properties of a pair of interacting neurofilaments. These properties allow us to understand the nature of interacting neurofilaments and may shed light into the behavior of sidearm-mediated NF interactions. The structural reorganizations of interacting NF pairs were examined under various conditions. To this end, we performed MC simulations of a pair of NFs by using the sequence-based coarse-grained NF brush model of Chang et al. [25]. The MC simulations were done under varying ionic conditions, phosphorylation state, and interfilament separations.

To reveal the conformational properties of interacting NFs, we employed different complementary measures that capture the behavior of interacting adjacent neurofilaments. Our analysis indicates that under salt-free conditions, apposing sidearms bend away from each other, forming a depletion region, a region that becomes large with increasing interfilament separation, at the center of the opposing filaments. It is interesting to point out that although the geometry is different, a similar behavior has been found in interacting spherical polyelectrolyte brushes (SPBs) (Fig. 8a) [42]. By using cryo-TEM experiments,

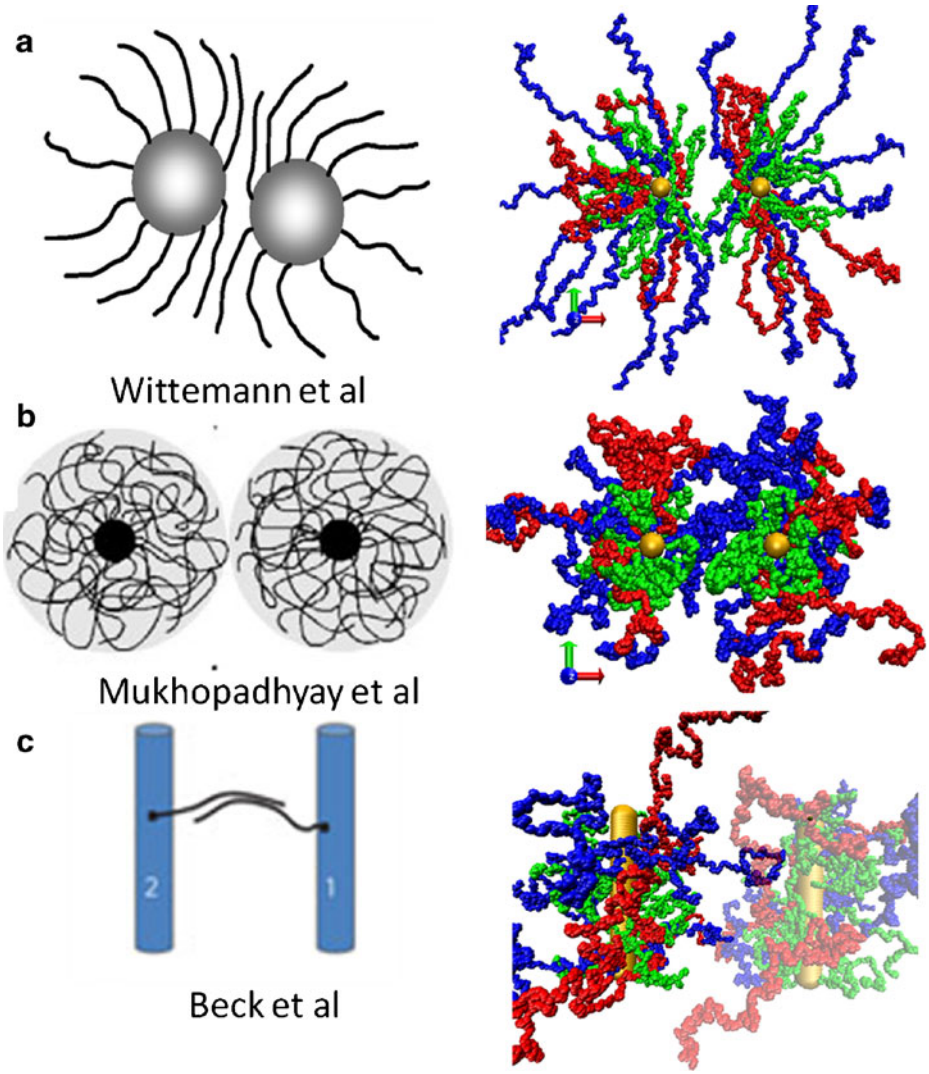

Fig. 8 Comparison of proposed models in the literature to the present study: **a** Interactions of spherical polymeric brush (SPBs) at low-ionic strength (Wittemnann et al. [42]) compared to the representative snapshot from the present MC simulation. The snapshot shows 40-nm-apart phosphorylated NF brush pair under salt-free condition. The schematic depiction on the left-hand side was adapted with permission from: Wittemann, A., M. Drechsler, et al. (2005). J. Am. Chem. Soc. 127(27): 9688–9689. Copyright @2005 American Chemical Society. **b** A schematic representation of the entropic brush model that was proposed by Brown and Hoh [44] as reviewed by Mukhopadhyay et al. [50] vs. a snapshot of 40-nm-apart phosphorylated NF brush pair under 150 mM of ionic solution. The schematic representation on the left-hand side was adapted from: Mukhopadhyay, R., S. Kumar, et al. (2004). Bioessays 26(9): 1017–1025., with permission from Wiley Interscience. **c** The 'handshake' sidearm interaction model proposed by Beck et al. [51] vs. a side view for representative snapshot of 40-nm-apart phosphorylated NF brush pair under 150 mM ionic strength. The schematic depiction on the left-hand side was adapted from Beck, R., J. Deek, et al. (2010). Nat. Mater. 9(1): 40–46 with permission from Nature

Wittemann et al. demonstrated that under low-ionic strength, the chains of the brush layers in two opposing SPBs bend away when the SPBs are close to each other [42]. This low-ionic strength behavior of SPBs resembles the observation in the salt-free condition of the present study (Fig. 8a), except for the additional polyampholytic nature of the present system.

To assess the conformations of interacting NF pairs under physiological conditions, we performed a set of MC simulations under 150 mM ionic solutions. The results from these simulations reveal significant conformational changes when compared to the salt-free conditions. Under ionic solution, the sidearms are found to adopt a coiled conformation in both phosphorylation states. A similar transition from a stretched to coiled conformation has been observed experimentally for the interacting SBPs mentioned above [42]. The authors demonstrated that the polyelectrolyte chains are strongly stretched under low-ionic strength and assume a coiled conformation under high-ionic strength, i.e., in the limit of the salted brush.

The change from the stretched, mutually excluding bent conformations to the coiled, interpenetrating conformations, suggests a change in the nature and type of interfilament interactions under ionic solution. In this regard, different mechanisms have been proposed to describe the interaction between neurofilaments. Based on the observation that NF sidearms are abundant with ionizable amino acid residues, sidearm-mediated interfilament interaction is described in terms of a repulsive electrostatic interaction [43]. In particular, the net-negative charges attained from serine phosphorylation of the KSP repeat motifs were considered to be responsible for sidearm-mediated NF interaction [39, 43]. The mutually exclusive type of conformation observed in the present study suggests apposing sidearms interact through electrostatic repulsive interactions under salt-free conditions.

Under 150 mM ionic solutions, the apposing sidearms were found in a coiled conformation. Clearly, this is the effect of the ionic screening. The electrostatic interaction would be short-ranged since the Debye screening length is $\sim$1 nm in 150 mM monovalent ionic solution. Therefore, from the observed coiled conformation, it would be reasonable to argue that the repulsive type of interaction is not a likely mechanism for NF-NF interactions under physiological ionic concentration. A similar conclusion was drawn by Brown and Hoh [44] based on the atomic force microscopy measurement of isolated NFs in the presence of co-isolating contaminants.

The experiment revealed the exclusion of co-assembled material from the proximity of the NF core and the presence of weak repulsive forces that extend for more than 50 nm from the filament core [44]. The authors then argued that such repulsion cannot be explained solely by electrostatic interaction that has a much shorter range due to the ionic screening [44]. They predicted that the thermally driven motion of sidearms results in an entropic brush and is responsible for regulating the interfilament spacing [44]. Others have argued interfilament interactions to be governed by the cross-bridge formation between adjacent filaments [45–48].

In the cross-bridge model, the non-covalent binding of NF sidearms, either by themselves or mediated by other accessory agents, is considered to be responsible for NF interactions. This hypothesis was originally based on electron microscopy (EM) studies of the frog axon where sidearms were found to form a dense network of cross-bridges that were 4–6 nm in diameter and 20–50 nm in length [46]. Some authors questioned these results by describing the cross-bridges as “artifacts” arising from the EM methods [49, 50], but a recent study by Beck et al. [51] supported cross-bridge interaction. The authors studied NF gels under varying pressure and revealed that NF gels undergo an abrupt transition from the gel expanded to the gel condensed state under high-osmotic pressure. Noting the

irreversibility of the gel-condensed state, the authors argued for an attractive interaction to overcome the repulsive interaction dominating the gel expanded state [51]. Then, they predicted NFs interact via attractive ionic cross-bridging of the polyampholyte sidearms in a 'handshaking' manner (cf. Fig. 8c).

In reference to cross-bridge interactions, our conformational analysis reveals a monotonically increasing overlapping probability (under ionic solutions) as the adjacent neurofilaments are compressed from 60 to 40 nm separations. However, from the snapshots and the average properties like density profile (cf. Figs. 2–4), the overlapping between the apposing sidearms does not appear to be in a 'hand-shake' manner as depicted in the cross-bridging model [51, 52] (refer to Fig. 8b and c for a comparison between proposed models of interacting NFs found in the literature (left panels) and snapshots of NF pairs from the MC simulations (right panel)). Nonetheless, it is interesting to point out that the density profiles shown in the present study exhibit close similarity to the conceptual drawings shown in Fig. 3e, f of Beck et al. [51], which were drawn to describe sidearm interactions under different compression levels.

It is important to emphasize that in spite of the increase in overlapping probability *I* as the interfilament distance is reduced from 60 to 40 nm, the absolute value of I is not significantly large (cf. Fig. 6a). From these observations, it is fair to speculate that the likelihood of cross-bridge interaction as the dominant mechanism for sidearm-mediated NF interaction is small. Instead, as proposed by Brown et al. [44], the conformational properties observed in the present study suggest entropic interaction as a likely mechanism for sidearm-mediated interactions under physiological conditions. However, to precisely resolve the mechanism of NF interactions, further investigation on the free energy and entropy of interacting filaments is warranted. Currently, efforts are underway along this direction.

In conclusion, the study of equilibrated NF pair conformations under different conditions reveals opposing sidearms from adjacent filaments do not interdigitate under salt-free conditions but rather bend away from each other forming a depletion region at the center. This suggests that the repulsive electrostatic interaction would be the dominant interaction for apposing sidearms under salt-free conditions. At the physiological salt concentration, opposing sidearms exhibit coiled conformations with increasing overlapping upon compression, suggesting that the entropic type of interaction may be dominant under physiological conditions.

Acknowledgement R.C. acknowledges support from the Korea Research Foundation (KRF) grant funded by the Korean government (MEST) (No. 2010–0003087) and the Kwangwoon Research Fund (2012) for this research.

References

1. Fuchs, E., Cleveland, D.W.: A structural scaffolding of intermediate filaments in health and disease. Science **279**(5350), 514–519 (1998)
2. Lee, M.K., Cleveland, D.W.: Neuronal intermediate filaments. Annu. Rev. Neurosci. **19**, 187–217 (1996)
3. Povlishock, J.T., Christman, C.W.: The pathobiology of traumatically induced axonal injury in animals and humans: a review of current thoughts. J. Neurotrauma **12**(4), 555–564 (1995)
4. Steinert, P.M., Roop, D.R.: Molecular and cellular biology of intermediate filaments. Annu. Rev. Biochem. **57**, 593–625 (1988)

5. Friede, R.L., Samorajski, T.: Axon caliber related to neurofilaments and microtubules in sciatic nerve fibers of rats and mice. Anat. Rec. **167**(4), 379–387 (1970)
6. Barry, D.M., Carpenter, C., Yager, C., Golik, B., Barry, K.J., Shen, H., Mikse, O., Eggert, L.S., Schulz, D.J., Garcia, M.L.: Variation of the neurofilament medium KSP repeat sub-domain across mammalian species: implications for altering axonal structure. J. Exp. Biol. **213**(1), 128–136 (2010)
7. Perrot, R., Berges, R., Bocquet, A., Eyer, J.: Review of the multiple aspects of neurofilament functions, and their possible contribution to neurodegeneration. Mol. Neurobiol. **38**(1), 27–65 (2008)
8. Delisle, M.B., Carpenter, S.: Neurofibrillary axonal swellings and amyotrophic lateral sclerosis. J. Neurol. Sci. **63**(2), 241–250 (1984)
9. Munoz, D.G., Greene, C., Perl, D.P., Selkoe, D.J.: Accumulation of phosphorylated neurofilaments in anterior horn motoneurons of amyotrophic lateral sclerosis patients. J. Neuropathol. Exp. Neurol. **47**(1), 9–18 (1988)
10. Goldman, J.E., Yen, S.H., Chiu, F.C., Peress, N.S.: Lewy bodies of Parkinson's disease contain neurofilament antigens. Science **221**(4615), 1082–1084 (1983)
11. Fabrizi, G.M., Cavallaro, T., Angiari, C., Cabrini, I., Taioli, F., Malerba, G., Bertolasi, L., Rizzuto, N.: Charcot-Marie-Tooth disease type 2E, a disorder of the cytoskeleton. Brain **130**(Pt 2), 394–403 (2007)
12. Donaghy, M., King, R.H., Thomas, P.K., Workman, J.M.: Abnormalities of the axonal cytoskeleton in giant axonal neuropathy. J. Neurocytol. **17**(2), 197–208 (1988)
13. Sternberger, N.H., Sternberger, L.A., Ulrich, J.: Aberrant neurofilament phosphorylation in Alzheimer disease. Proc. Natl. Acad. Sci. U. S. A. **82**(12), 4274–4276 (1985)
14. Ishii, T., Haga, S., Tokutake, S.: Presence of neurofilament protein in Alzheimer's neurofibrillary tangles (ANT). An immunofluorescent study. Acta Neuropathol. **48**(2), 105–112 (1979)
15. Geisler, N., Kaufmann, E., Fischer, S., Plessmann, U., Weber, K.: Neurofilament architecture combines structural principles of intermediate filaments with carboxy-terminal extensions increasing in size between triplet proteins. EMBO J. **2**(8), 1295–1302 (1983)
16. Yuan, A., Rao, M.V., Sasaki, T., Chen, Y., Kumar, A., Veeranna, Liem, R.K., Eyer, J., Peterson, A.C., Julien, J.P., Nixon, R.A.: Alpha-internexin is structurally and functionally associated with the neurofilament triplet proteins in the mature CNS. J. Neurosci. **26**(39), 10006–10019 (2006)
17. Yuan, A., Sasaki, T., Kumar, A., Peterhoff, C.M., Rao, M.V., Liem, R.K., Julien, J.P., Nixon, R.A.: Peripherin is a subunit of peripheral nerve neurofilaments: implications for differential vulnerability of CNS and peripheral nervous system axons. J. Neurosci. **32**(25), 8501–8508 (2012)
18. Carpenter, D.A., Wallace, l.: Neurofilament triplet protein interactions: evidence for the preferred formation of NF-L-containing dimers and a putative function for the end domains. J. Cell Sci. **109**(Pt 10), 2493–2498 (1996)
19. Janmey, P.A., Leterrier, J.F., Herrmann, H.: Assembly and structure of neurofilaments. Curr. Opin. Colloid Interface Sci. **8**(1), 40–47 (2003)
20. Jacomy, H., Zhu, Q., Couillard-Despres, S., Beaulieu, J.M., Julien, J.P.: Disruption of type IV intermediate filament network in mice lacking the neurofilament medium and heavy subunits. J. Neurochem. **73**(3), 972–984 (1999)
21. Carter, J., Gragerov, A., Konvicka, K., Elder, G., Weinstein, H., Lazzarini, R.A.: Neurofilament (NF) assembly; divergent characteristics of human and rodent NF-L subunits. J. Biol. Chem. **273**(9), 5101–5108 (1998)
22. Heins, S., Wong, P.C., Muller, S., Goldie, K., Cleveland, D.W., Aebi, U.: The rod domain of NF-L determines neurofilament architecture, whereas the end domains specify filament assembly and network formation. J. Cell Biol. **123**(6 Pt 1), 1517–1533 (1993)
23. Stevens, M.J., Hoh, J.H.: Interactions between planar grafted neurofilament side-arms. J. Phys. Chem., B **115**(23), 7541–7549 (2011)
24. Zhulina, E.B., Leermakers, F.A.: A self-consistent field analysis of the neurofilament brush with amino-acid resolution. Biophys. J. **93**(5), 1421–1430 (2007)
25. Chang, R., Kwak, Y., Gebremichael, Y.: Structural properties of neurofilament sidearms: sequence-based modeling of neurofilament architecture. J. Mol. Biol. **391**(3), 648–660 (2009)
26. Qianqian Cao, C.Z., He, H., Li, L.: A molecular dynamics study of two apposing polyelectrolyte brushes with mono and multivalent counterions. Macromol. Theory Simul. **18**, 441–452 (2009)
27. Korobko, A.V., Jesse, W., Egelhaaf, S.U., Lapp, A., van der Maarel, J.R.: Do spherical polyelectrolyte brushes interdigitate? Phys. Rev. Lett. **93**(17), 177801 (2004)
28. Stevenson, W., Chang, R., Gebremichael, Y.: Phosphorylation-mediated conformational changes in the mouse neurofilament architecture: insight from a neurofilament brush model. J. Mol. Biol. **405**(4), 1101–1118 (2011)
29. McQuarrie, D.A.: Statistical Mechanics. University Science Books, Sausalito, CA (2000)

30. Smit, B., Fenkel, D.: Understanding Molecular Simulation: From Algorithms to Applications, Computational Science Series, vol. 1, 2nd edn. Academic Press, San Diego, CA (2002)
31. Xu, Z., Marszalek, J.R., Lee, M.K., Wong, P.C., Folmer, J., Crawford, T.O., Hsieh, S.T., Griffin, J.W., Cleveland, D.W.: Subunit composition of neurofilaments specifies axonal diameter. J. Cell Biol. **133**(5), 1061–1069 (1996)
32. Kumar, S., Hoh, J.H.: Modulation of repulsive forces between neurofilaments by sidearm phosphorylation. Biochem. Biophys. Res. Commun. **324**(2), 489–496 (2004)
33. Hsieh, S.T., Crawford, T.O., Griffin, J.W.: Neurofilament distribution and organization in the myelinated axons of the peripheral nervous-system. Brain Res. **642**(1–2), 316–326 (1994)
34. Martin, R., Door, R., Ziegler, A., Warchol, W., Hahn, J., Breitig, D.: Neurofilament phosphorylation and axon diameter in the squid giant fibre system. Neuroscience **88**(1), 327–336 (1999)
35. Glicksman, M.A., Soppet, D., Willard, M.B.: Posttranslational modification of neurofilament polypeptides in rabbit retina. J. Neurobiol. **18**(2), 167–196 (1987)
36. Nixon, R.A., Paskevich, P.A., Sihag, R.K., Thayer, C.Y.: Phosphorylation on carboxyl terminus domains of neurofilament proteins in retinal ganglion cell neurons in vivo: influences on regional neurofilament accumulation, interneurofilament spacing, and axon caliber. J. Cell Biol. **126**(4), 1031–1046 (1994)
37. Hsieh, S.T., Kidd, G.J., Crawford, T.O., Xu, Z.S., Lin, W.M., Trapp, B.D., Cleveland, D.W., Griffin, J.W.: Regional modulation of neurofilament organization by myelination in normal axons. J. Neurosci. **14**(11), 6392–6401 (1994)
38. Carden, M.J., Trojanowski, J.Q., Schlaepfer, W.W., Lee, V.M.: Two-stage expression of neurofilament polypeptides during rat neurogenesis with early establishment of adult phosphorylation patterns. J. Neurosci. **7**(11), 3489–3504 (1987)
39. Dewaegh, S.M., Lee, V.M.Y., Brady, S.T.: Local modulation of Neurofilament phosphorylation, axonal caliber, and slow axonal-transport by myelinating Schwann-cells. Cell **68**(3), 451–463 (1992)
40. Panwar, A.S., Kumar, S.: Brownian dynamics simulations of polyelectrolyte adsorption in shear flow. J. Chem. Phys. **122**(15), 154902 (2005)
41. Frishchknecht, A.L.: Forces between nanorods with end-adsorbed chains in a homopolymer melt. J. Chem. Phys. **128**(22), 224902 (2008)
42. Wittemann, A., Drechsler, M., Talmon, Y., Ballauff, M.: High elongation of polyelectrolyte chains in the osmotic limit of spherical polyelectrolyte brushes: a study by cryogenic transmission electron microscopy. J. Am. Chem. Soc. **127**(27), 9688–9689 (2005)
43. Carden, M.J., Trojanowski, J.Q., Schlaepfer, W.W., Lee, V.M.: Two-stage expression of neurofilament polypeptides during rat neurogenesis with early establishment of adult phosphorylation patterns. J. Neurosci. **7**(11), 3489–3504 (1987)
44. Brown, H.G., Hoh, J.H.: Entropic exclusion by neurofilament sidearms: a mechanism for maintaining interfilament spacing. Biochemistry **36**(49), 15035–15040 (1997)
45. Hirokawa, N., Glicksman, M.A., Willard, M.B.: Organization of mammalian neurofilament polypeptides within the neuronal cytoskeleton. J. Cell Biol. **98**(4), 1523–1536 (1984)
46. Hirokawa, N.: Cross-linker system between neurofilaments, microtubules, and membranous organelles in frog axons revealed by the quick-freeze, deep-etching method. J. Cell Biol. **94**(1), 129–142 (1982)
47. Leterrier, J.F., Kas, J., Hartwig, J., Vegners, R., Janmey, P.A.: Mechanical effects of neurofilament cross-bridges—modulation by phosphorylation, lipids, and interactions with F-actin. J. Biol. Chem. **271**(26), 15687–15694 (1996)
48. Letterier, J.F., Eyre, J.: Properties of highly viscous gels formed by neurofilament in vitro: a possible consequence of a specific inter-filament cross-bridging. Biochem. J. **245**, 93–101 (1987)
49. Price, R.L., Paggi, P., Lasek, R.J., Katz, M.J.: Neurofilaments are spaced randomly in the radial dimension of axons. J. Neurocytol. **17**(1), 55–62 (1988)
50. Mukhopadhyay, R., Kumar, S., Hoh, J.H.: Molecular mechanisms for organizing the neuronal cytoskeleton. BioEssays **26**(9), 1017–1025 (2004)
51. Beck, R., Deek, J., Jones, J.B., Safinya, C.R.: Gel-expanded to gel-condensed transition in neurofilament networks revealed by direct force measurements. Nat. Mater. **9**(1), 40–46 (2010)
52. Gou, J.P., Gotow, T., Janmey, P.A., Leterrier, J.F.: Regulation of neurofilament interactions in vitro by natural and synthetic polypeptides sharing Lys-Ser-Pro sequences with the heavy neurofilament subunit NF-H: neurofilament crossbridging by antiparallel sidearm overlapping. Med. Biol. Eng. Comput. **36**(3), 371–387 (1998)